Supporting Information

Sensitized near infrared lanthanide emission in chalcogenide perovskites.

Jinan H. Al Shuhaib, Isabel J. Ferrer, José R. Ares, Salvatore Cianci, Federico Tuzi, Elena Blundo, Antonio Polimeni, Antonio Benayas, Riccardo Marin, Fabrice Leardini

Table of Contents

S1. Optimization of the sulfurization process.

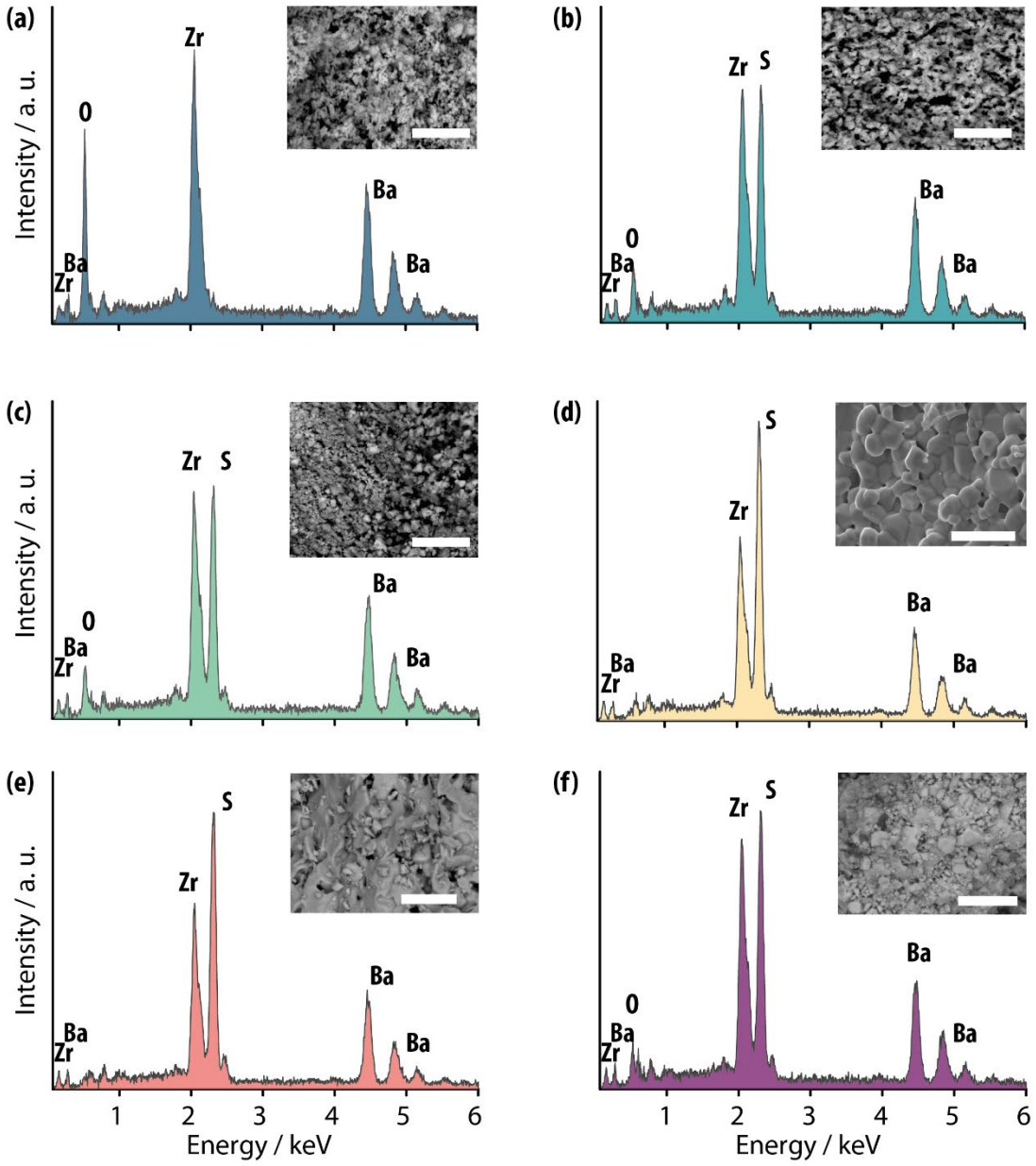

Figure S1. EDX spectra of (a) BZO, (b) BZS-900, (c) BZS-950, (d) BZS-1000, (e) BZS-1050 and (f) BZS-1100. The insets show the SEM images of the corresponding samples. The scale bar is 10 μm in all images.

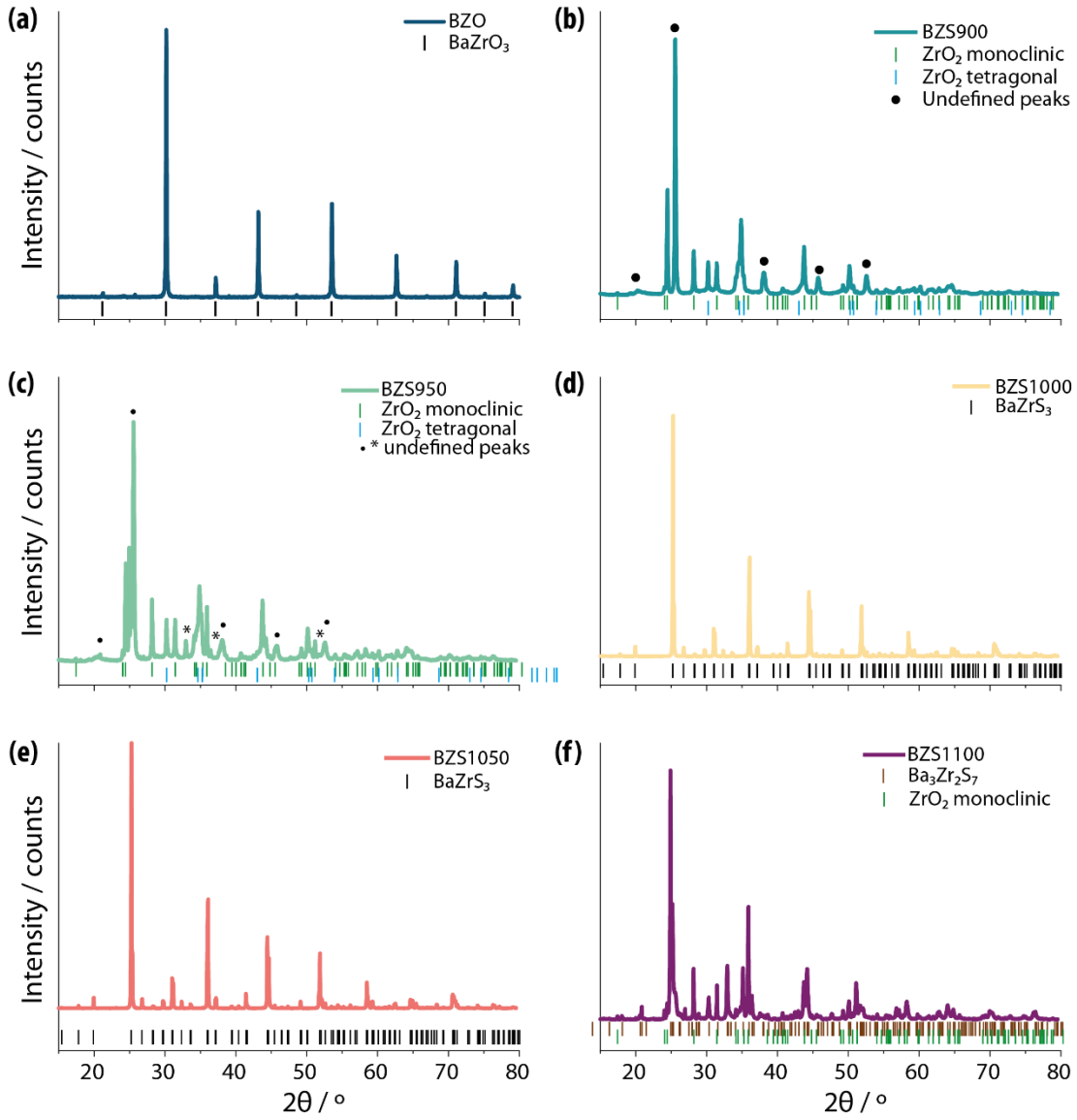

Figure S2. XRPD diffraction patterns of: (a) BZO, all peaks can be indexed to the space group $Pm\bar{3}m$ (JCPDS 96-153-2744). (b) BZS-900 and (c) BZS-950. Both diffraction patterns present unidentified peaks coming presumably from a dominant undefined phase, as well as peaks related to monoclinic ZrO_2 (with space group of *P21/C*) and tetragonal ZrO_2 (with space group of *P42/nmc*) that matched the standard files JCPDS 01-078-1807 and 01-080-0784, respectively. (d) BZS-1000 and (e) BZS1050. Both patterns match the standard file JCPDS 01-073-0847, corresponding to $BaZrS_3$ phase. (f) BZS1100 that matches the standard files JCPDS 01-078-1807 and JCPDS 01-080-1999, corresponding to monoclinic ZrO_2 and to the $Ba_3Zr_2S_7$ Ruddlesden-Popper phase.

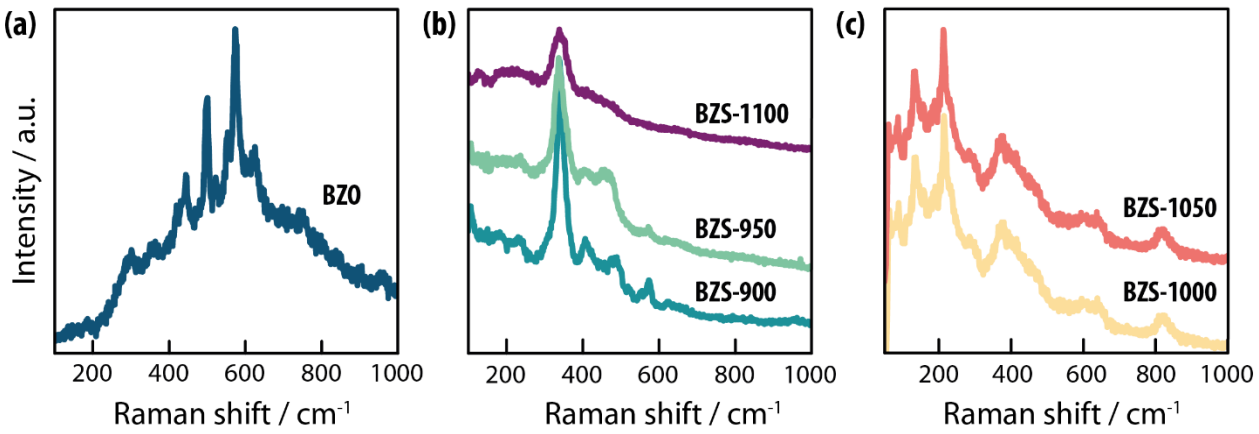

Figure S3. Raman spectra of (a) $BaZrO_3$, (b) samples containing the ZrO_2 phase (BZS-900, BZS-950 and BZS-1100) and (c) samples containing $BaZrS_3$ phase (BZS-1000 and BZS-1050).

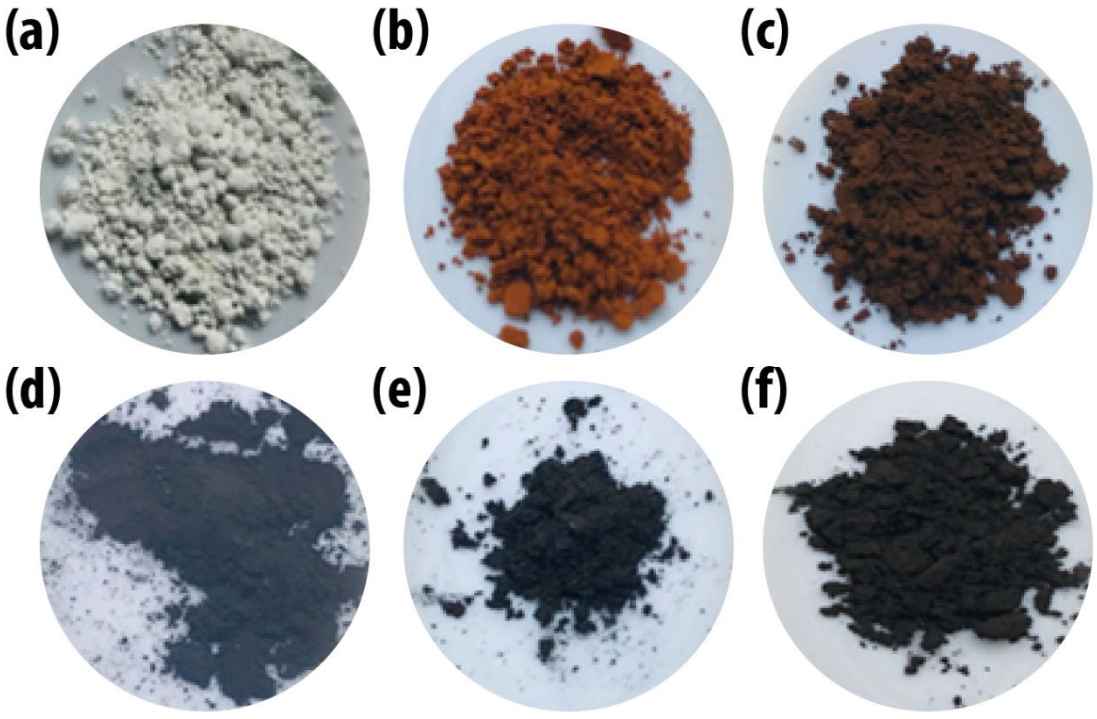

Figure S4. Pictures of (a) BZO, (b) BZS-900, (c) BZS-950, (d) BZS-1000, (e) BZS-1050 and (f) BZS-1100 powders.

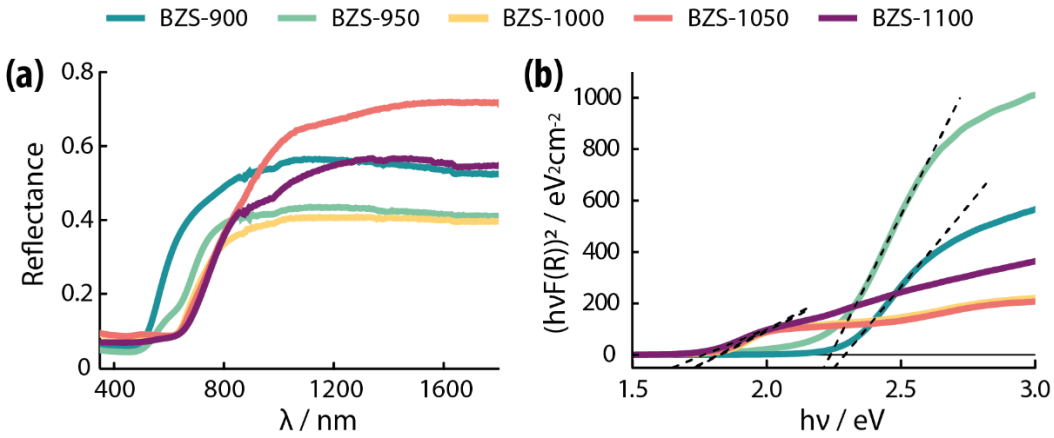

Figure S5. Diffuse reflectance spectra (a) and Tauc plots obtained from the corresponding Kubelka-Munk functions (b) of the BZS-series. The black dashed lines are the linear fits used to calculate the optical energy bandgaps. Different Tauc plots were checked by considering direct/indirect-allowed/forbidden transitions. Best fits were obtained by considering direct allowed transitions. From this Tauc analysis it becomes evident that the optical bandgap shifts to lower values when increasing the sulfurization temperature from 900 to 1000 ºC and then stabilizes. The optical bandgaps of the undefined phases of BZS-900 and BZS-950 samples lie in the visible region and are different (2.29±0.06 eV and 2.23±0.06 eV, respectively), suggesting that both samples have dissimilar composition and thus different optical properties. The optical bandgaps further decrease to about 1.76±0.06 eV for BZS-1000 and BZS-1050 samples, in good agreement with reported data for the $BaZrS_3$ phase, which span between 1.73 and 1.85 eV [1, 2]. Finally, the optical bandgap of the $Ba_3Zr_2S_7$ phase is quite similar to that obtained for the $BaZrS_3$ phase, namely 1.76±0.04 eV. That value differs from previous theoretical predictions for that phase that computed an indirect transition with a bandgap energy of 1.25 eV [3, 4]. As far as we know no experimental results have been reported up to date for the optical bandgap of the Ruddlesden–Popper phase.

S2. Stability of the material.

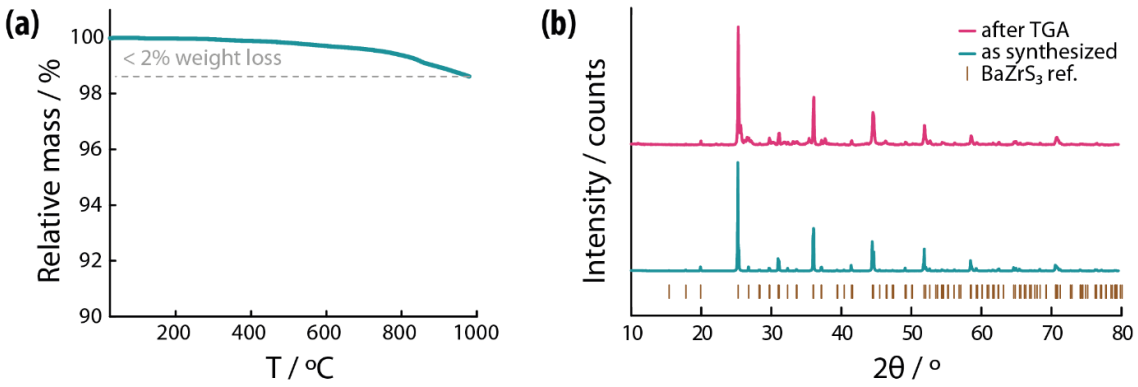

Figure S6. (a) Relative mass recorded during TGA run of BZS-1050 sample under Ar flow. (b) XRPD pattern of the as prepared sample and the one obtained after the TGA run. Vertical lines indicate the peak positions of $BaZrS_3$ phase with an orthorhombic distorted perovskite structure belonging to the space group *Pnma* (JCPDS 01-073-0847). It can be seen that the main phase appearing in the sample after the TGA measurement is still BaZrS3, although there are minor additional peaks that could be tentatively ascribed to the $BaCO_3$ and ZrO_2 (formed by reaction with O_2 and CO_2 traces present in the gas line) and to thermal decomposition of $BaZrS_3$ into $Ba_3Zr_2S_7$.

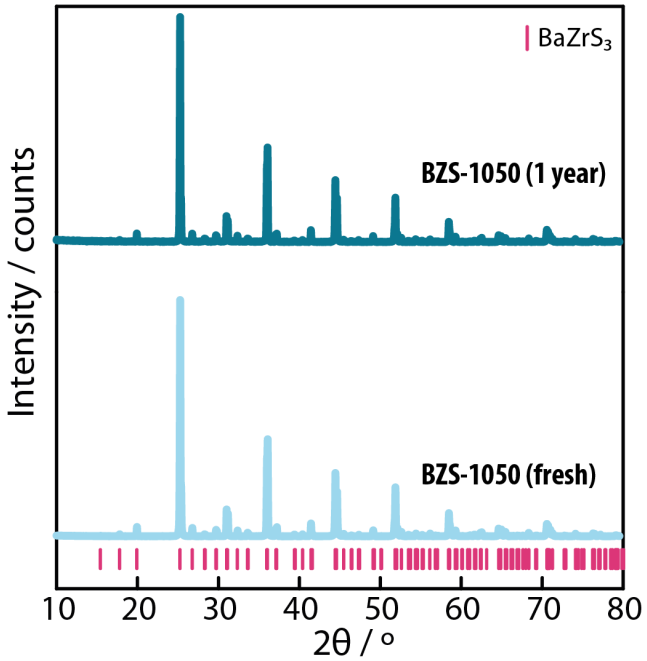

Figure S7. XRPD pattern of as prepared BZS-1050 sample and after air exposure for one year. Vertical lines indicate the peak positions of $BaZrS_3$ phase with an orthorhombic distorted perovskite structure belonging to the space group *Pnma* (JCPDS 01-073-0847).

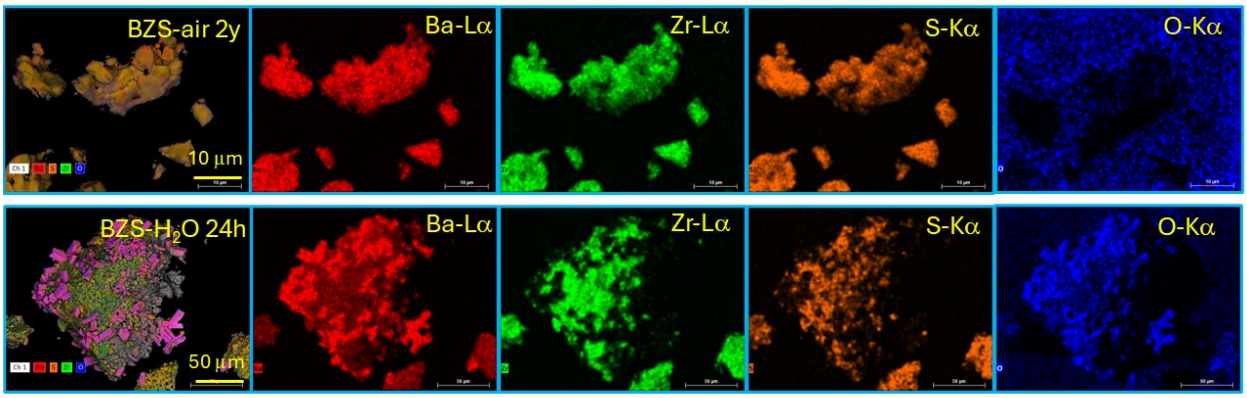

Figure S8. EDX maps (showing relevant X-ray emission lines for Ba, Zr, S and O) of BZS-1050 powders after air exposure for 2 years (top panel) and after water (MilliQ-grade) exposure for 24 h (bottom panel). Left-side images are obtained by the combination of the different single-colored images. The combined image for air-exposed BZS shows a uniform color, indicating good compositional homogeneity. In that sample, O-Kα signal from the sample holder is also observed, due to the low O-content in the BZS powders. On the contrary, a clear oxidation of the powders is observed after water immersion (as evidenced by the O-Kα signal), giving rise to segregation of oxygen-rich Ba phases forming prismatic crystals and S-containing Zr-rich phases.

S3. Additional characterization of the Ln^{3+}-doped materials.

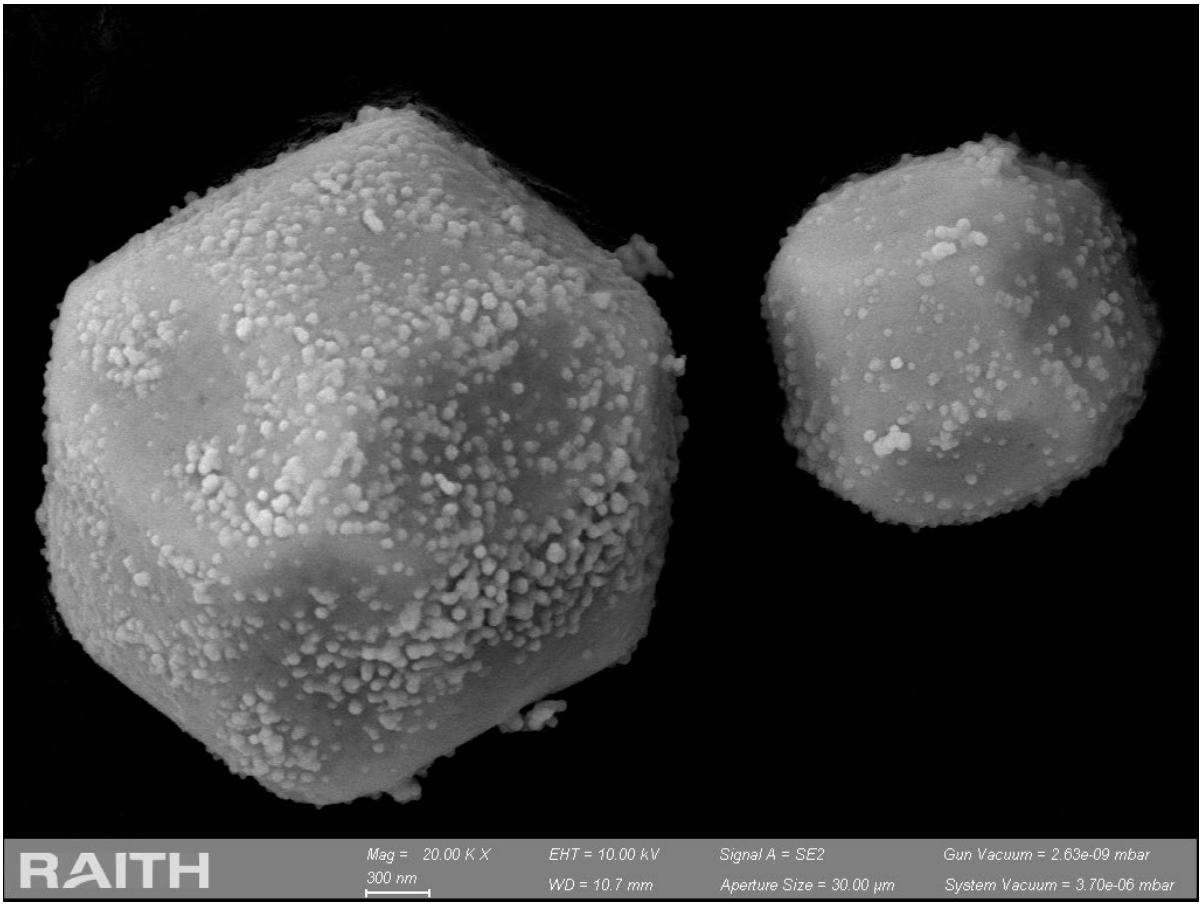

Figure S9. High/magnification SEM image of BZO-Er sample, showing the decaoctahedral morphology typical of this material.

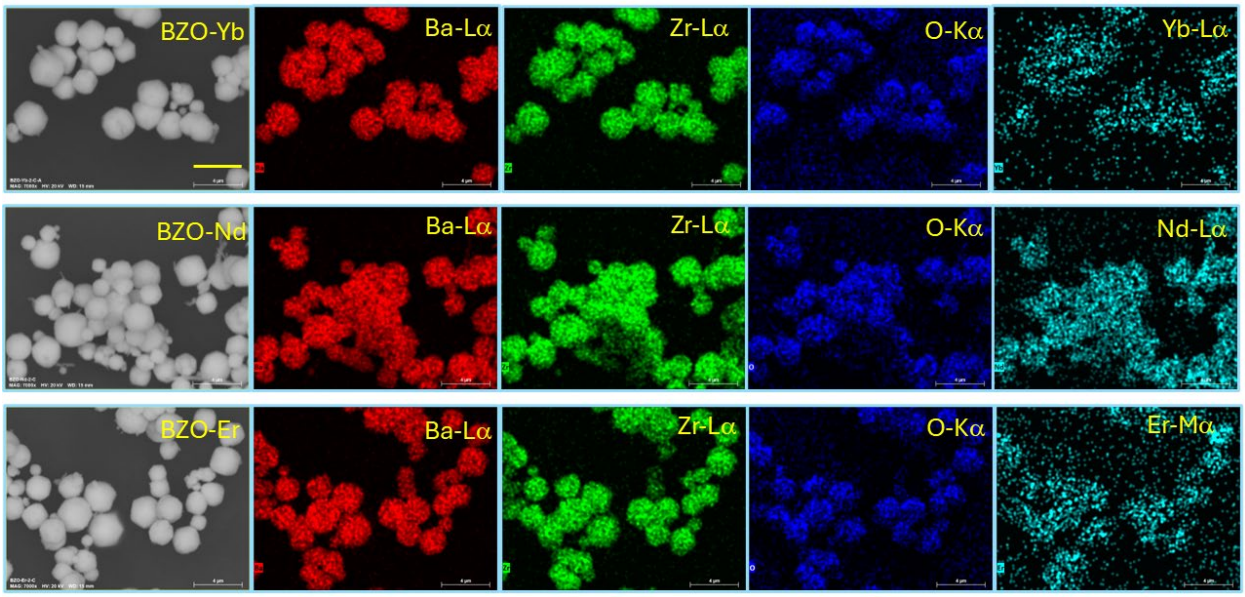

Figure S10. Back-scattered electron images and EDX maps (showing relevant X-ray emission lines for each element) of BZO-Ln series. Top panel: BZO-Yb powders, middle panel: BZO-Nd and bottom panel: BZO-Er. The scale bar is 4 μm in all images.

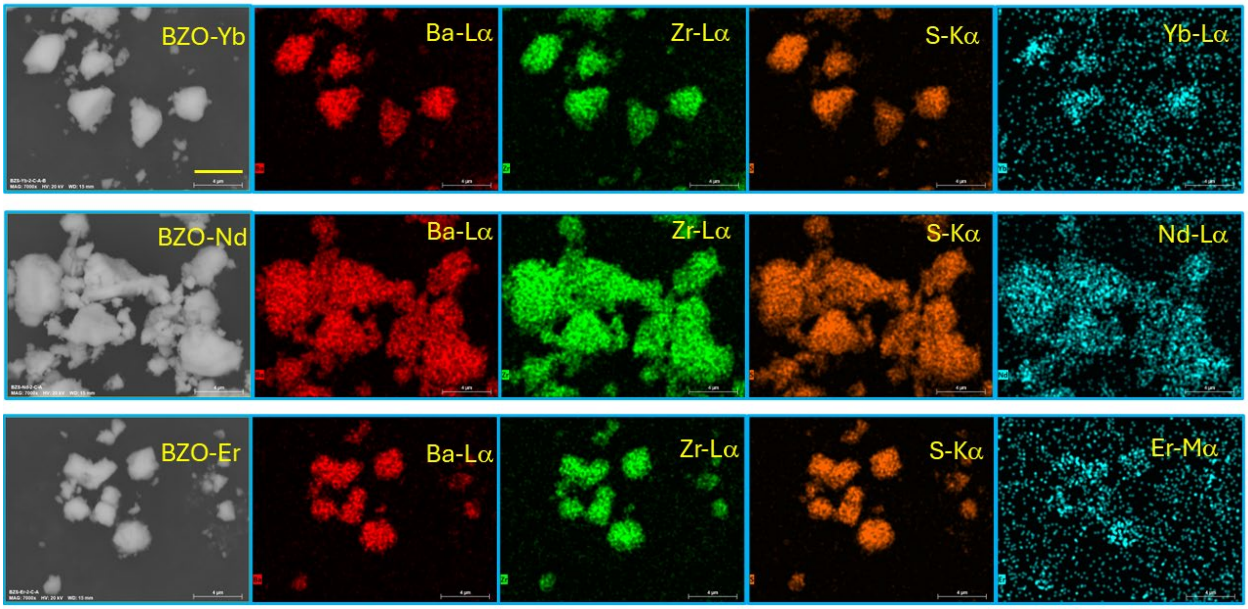

Figure S11. Back scattered electron images and EDX maps (showing relevant x-ray emission lines for each element) of BZS-Ln series. Top panel: BZS-Yb powders, middle panel: BZS-Nd and bottom panel: BZS-Er. The scale bar is 4 μm in all images.

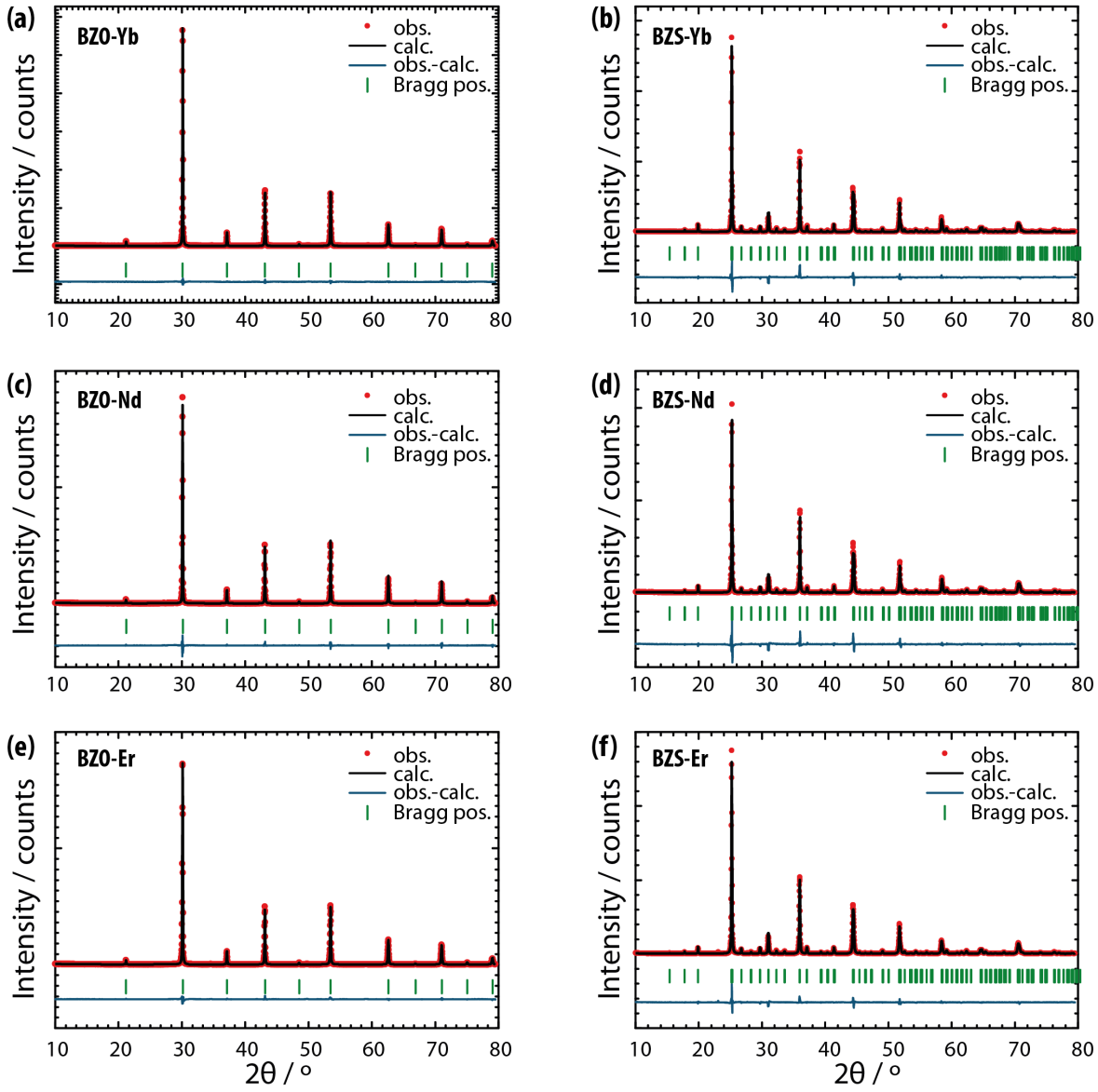

Figure S12. XRPD patterns (red points) of (a) BZO-Yb, (b) BZS-Yb, (c) BZO-Nd, (d) BZS-Nd, (e) BZS-Er, (f) BZS-Er samples. Black lines are the Rietveld refinements of the patterns, whereas the blue lines represent the differences between experimental and refined patterns. Peak positions of Bragg peaks are indicated by vertical green lines.

Table S1. Lattice parameters, unit cell volume and chi-square fitting value obtained in Rietveld refinements of undoped and Ln^{3+}-doped $BaZrO_3$ samples.

Sample name	a (Å)	V (Å^3)	χ^2
BZO	4.1918(1)	73.655	2.46
BZO-Nd	4.1933(1)	73.732	3.46
BZO-Er	4.1941(1)	73.777	3.32
BZO-Yb	4.1944(1)	73.790	3.65
$BaZrO_3$ [5]	4.193		
$BaZrO_3$ [6]	4.1943		

Table S2. Lattice parameters, unit cell volume and chi-square fitting value obtained from the Rietveld refinements of undoped and Ln^{3+}-doped $BaZrS_3$ samples.

Sample name	a (Å)	b (Å)	c (Å)	V (Å^3)	χ2
BZS-1000	7.0659	9.9824	7.0189	495.08	3.72
BZS-Nd	7.0651	9.9799	7.0286	495.58	6.85
BZS-Er	7.0672	9.9911	7.0393	497.04	4.21
BZS-Yb	7.0708	9.9920	7.0311	496.76	6.71
$BaZrS_3$ [7]	7.061	9.977	7.014	494.1	1.07
$BaZrS_3$ [8]	7.0599	9.9813	7.0251	495.04	

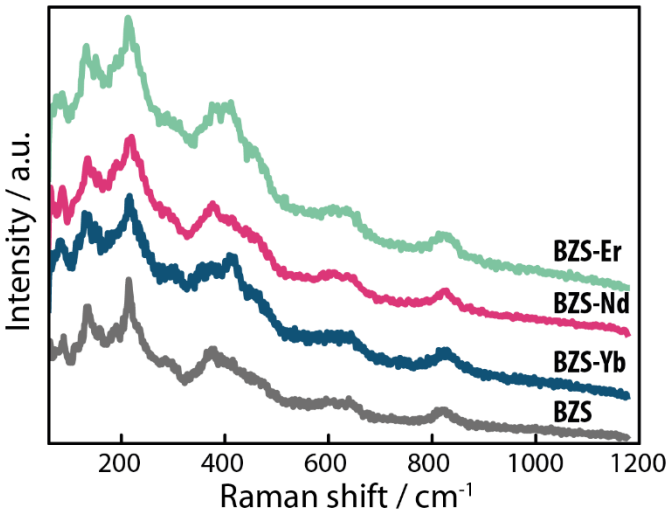

Figure S13. Raman spectra of the BZS-Ln series and BZS-1000. The spectra have been vertically shifted to allow a better comparison.

Table S3. Wavenumber values (cm^{-1}) of the Raman bands observed for undoped and Ln^{3+}-doped BZS powders.

Assignment	BZS-1000	BZS-Yb	BZS-Er	BZS-Nd	Ref [9]	Ref [10]	Ref [11]	Ref [12]
A_g^1	60	62	60	62	60	60	60	60
B_{1g}^1	90	83	82	85	90	90	87	85
A_g^4	130	135	133	134	130	130	130	140
B_{2g}^6	215	215	212	210	220	210	210	230
B_{1g}^5	390	400	380	380	390	400	400	410
	----	412	410	410		--	--	
E_g(BZO)	615	615	615	630		--	--	620
B_{1g}^5(2^{nd}order)	820	825	825	825		--		820

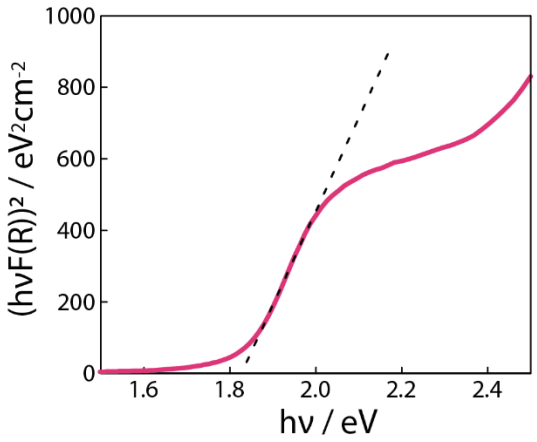

Figure S14. Tauc plot of the BZS-Yb sample (representative of the BZS-Ln series) obtained from the diffuse reflectance spectroscopy measurements (F(R) represents the Kubelka-Munk function). The dashed line is the linear fit used to calculate the optical bandgap.

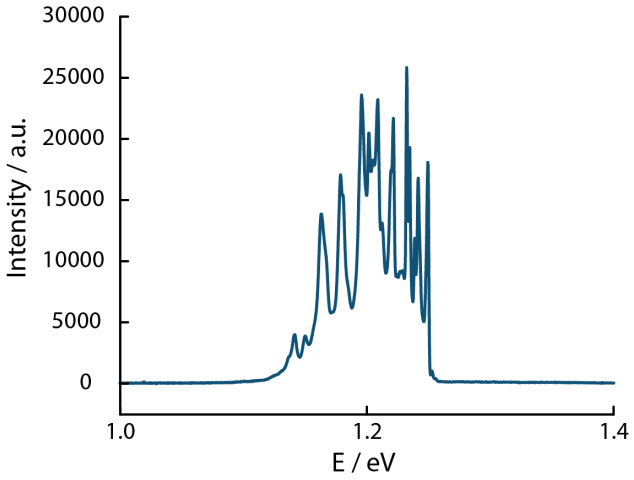

Figure S15. Photoluminescence of BSZ-Yb at 10 K under 405-nm excitation.

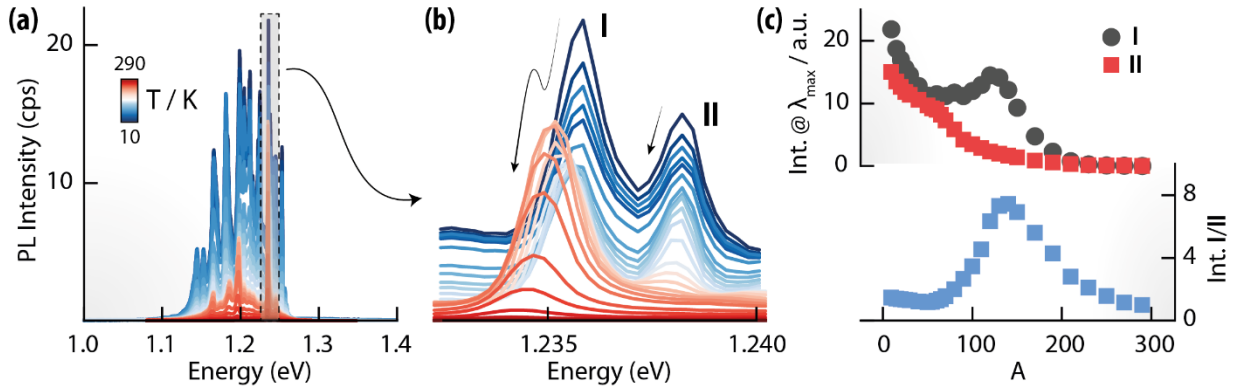

Figure S16. (a) Photoluminescence spectra of BSZ-Yb collected under 532-nm excitation as a function of temperature. (b) A zoom-in of the Yb^{3+}:$^2F_{5/2} \rightarrow {}^2F_{7/2}$ emission band shows a different trend of what appear to be two Stark components (**I** and **II**). (c) The analysis of the intensity of the maximum of **I** and **II** shows that **I** undergoes thermal anti-quenching between 70 and 120 K, while **II** follows a more typical monotone thermal quenching along the whole range of explored temperatures. This observation, paired with the fact that at least 12 components could be counted in the emission of Yb^{3+} at 10 K – way more than the expected 4 Staks levels expected for the Yb^{3+}:$^2F_{5/2} \rightarrow {}^2F_{7/2}$ band – suggests that multiple Yb^{3+} populations are present in the crystal structure. This is not surprising, considering three factors. First, there is a charge mismatch between Zr^{4+} and Ln^{3+}. Hence substitutional doping is bound to introduce defects and, hence, disorder in the structure. Second, $BaZrS_3$ is S-deficient. Thus, different defects are expected to be found at different crystal locations. Third, Ln^{3+} could also occupy the A-site. Because of the above, it is not surprising that multiple Yb^{3+} populations are present in the crystal, each subjected to different quenching (or antiquenching) processes that depend on the local crystal environment.

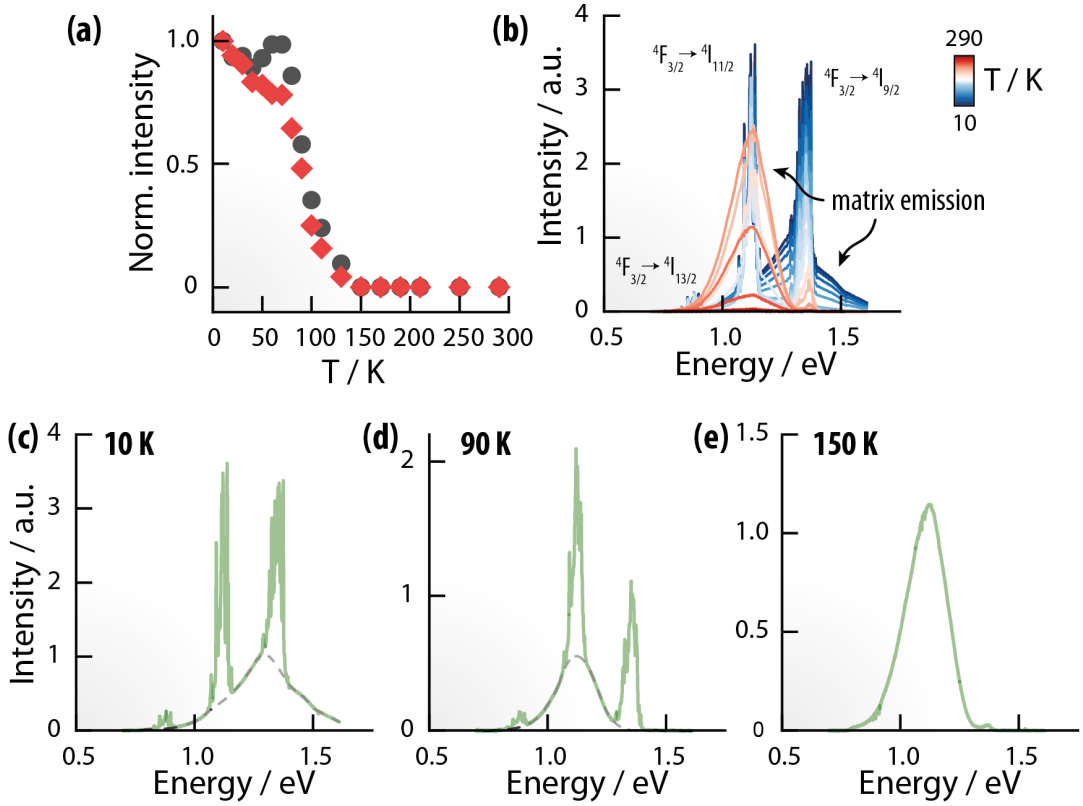

Figure S17. (a) Intensity vs temperature for the Nd^{3+}:$^4F_{3/2} \rightarrow {}^4I_{11/2}$ (red) and Nd^{3+}:$^4F_{3/2} \rightarrow {}^4I_{9/2}$ (grey) bands. The integrated intensity was obtained from the dataset shown in (b) – recorded under 405-nm excitation – after manually subtracting the broad emission coming from the matrix as shown in (c) and (d). Only matrix emission is observed increasing the temperature to reach 150 K (e). The intensity vs temperature plot shown in **Figure 4g** of the main manuscript was obtained from the average of the 2 datasets in (a) to account for inaccuracies in the treatment in the manual subtraction of the broad signals. Like in the case of BZS-Yb, the number of Stark levels observed in Nd^{3+} emissions is higher than the expected one (e.g., at least 15 components are observed for the Nd^{3+}:$^4F_{3/2} \rightarrow {}^4I_{11/2}$ transition instead of the expected 6). This is, again, an indication of multiple Ln^{3+} populations.

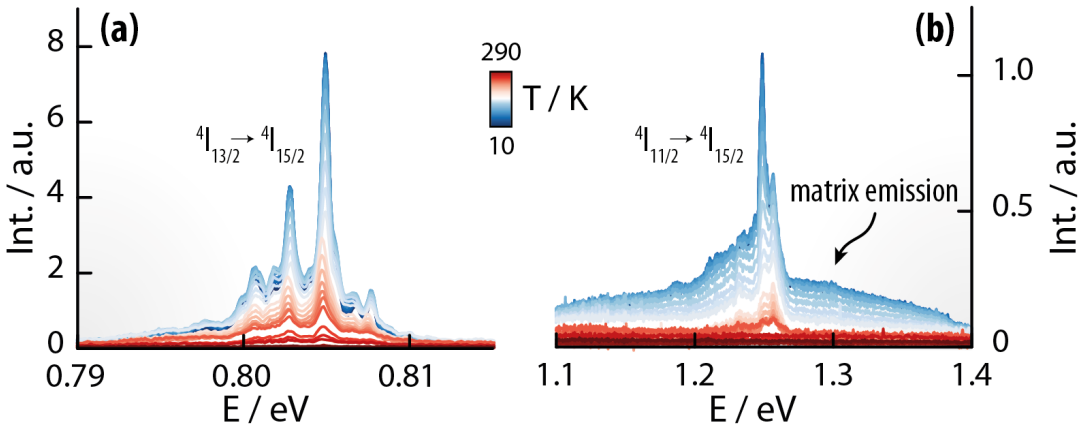

Figure S18. Zoom in of the Er^{3+}:$^4I_{13/2}$ → $^4I_{15/2}$ (a) and Er^{3+}:$^4I_{13/2}$ → $^4I_{15/2}$ (b) transitions measured at different temperatures exciting BZS-Er at 405 nm. The Er^{3+}:$^4I_{13/2}$ → $^4I_{15/2}$ transition was integrated to obtain the trend of intensity vs temperature in **Figure 4i** of the main manuscript, given its lack of overlap with the emission from the matrix.

Table S4. Values of the parameters used for the Mott-Seitz fits reported in **Figure 4** of the main manuscript.

Sample name	α_1	ΔE_1 / cm^{-1} (meV)	α_2	ΔE_2 / cm^{-1} (meV)	χ^2
BZS-1000	70	161 (20)	15864	1306 (161)	0.994
BZS-Yb	17	107 (13)	$1.14 \cdot 10^7$	1834 (227)	0.996
BZS-Nd	$3.56 \cdot 10^7$	583 (72)	-	-	0.988
BZS-Er	78	245 (30)	3311	1019 (126)	0.994

References

[1] Niu, S.; *et al.* Bandgap Control via Structural and Chemical Tuning of Transition Metal Perovskite Chalcogenides. *Adv. Mater.*, **2017**, 29, 1604733.

[2] Nishigaki, Y.; *et al*. Extraordinary Strong Band-Edge Absorption in Distorted Chalcogenide Perovskites. *Sol. RRL*, **2020**, 4, 1900555.

[3] Niu, S.; *et al.* Optimal Bandgap in a 2D Ruddlesden–Popper Perovskite Chalcogenide for Single-Junction Solar Cells. *Chem. Mater.* **2018**, 30, 4882−4886.

[4] Li, Y.; Singh, D.J.; Tunability of electronic and optical properties of the Ba–Zr–S system via dimensional reduction. *Eur. Phys. J. B*, **2018**, 91, 188.

[5] Swanson, H.E.; Gilfrich, N.T.; Ugrinic, G.M. Standard X ray diffraction powder patterns. *Natl. Bur. Stand. (US)*, **1955**, Circular 539, V, 8.

[6] Levin, I.; Amos, T.G.; Bell, S.M.; Farber, L.; Vanderah, T.A.; Roth, R.S.; Toby, B.H. Phase equilibria, crystal structures and dielectric anomaly in the BaZrO3-CaZrO3 system. *J. Solid State Chemistry*, **2003**, 165, 160-181.

[7] Niu, S.; *et al.* Bandgap Control via Structural and Chemical Tuning of Transition Metal Perovskite Chalcogenides. *Adv. Mater.*, **2017**, 29, 1604733.

[8] Lelieveld, R.; IJdo, D. J. W. Sulphides with the $GdFeO_3$ structure. *Acta Crystallographica Section B*, **1980**, 36, 2223-2226.

[9] Wei, X.; et al. Realization of BaZrS3 chalcogenide perovskite thin films for optoelectronics. *Nano Energy*, **2020**, 68, 104317.

[10] Perera, S.; *et al.* Chalcogenide perovskites – an emerging class of ionic semiconductors. *Nano energy*, **2016**, 22, 129–135.

[11] Gross, N.; Sun, Y.-Y.; Perera, S.; Hui, H.; Wei, X.; Zhang, S.; Zeng, H.; Weinstein, B.A. Stability and Band-Gap Tuning of the Chalcogenide Perovskite $BaZrS_3$ in Raman and Optical Investigations at High Pressures. *Phys. Rev. Appl.*, **2017**, 8, 044014.

[12] Pandey, J.; Ghoshal, D.; Dey, D.; Gupta, T.; Taraphder, A.; Koratkar, N.; Soni, A. Local ferroelectric polarization in antiferroelectric chalcogenide perovskite $BaZrS_3$ thin films. *Phys. Rev. B*, **2020**, 102, 205308.